First-principles calculation of shift current in chalcopyrite semiconductor $ZnSnP_2$

Banasree Sadhukhan,[1,*] Yang Zhang,[1,2,3] Rajyavardhan Ray,[1,4,†] and Jeroen van den Brink[1,4]

[1]*Leibniz Institute for Solid State and Materials Research IFW Dresden, Helmholtzstrasse 20, 01069 Dresden, Germany*

[2]*Department of Physics, Massachusetts Institute of Technology, Cambridge, Massachusetts 02139, USA*

[3]*Max Planck Institute for Chemical Physics of Solids, 01187 Dresden, Germany*

[4]*Dresden Center for Computational Materials Science, TU Dresden, D-01062 Dresden, Germany*

(Received 8 November 2019; accepted 5 May 2020; published 2 June 2020)

The bulk photovoltaic effect generates intrinsic photocurrents in materials without inversion symmetry. Shift current is one of the bulk photovoltaic phenomena related to the Berry phase of the constituting electronic bands: photoexcited carriers coherently shift in real space due to the difference in the Berry connection between the valence and conduction bands. Ferroelectric semiconductors and Weyl semimetals are known to exhibit such nonlinear optical phenomena. Here we consider the chalcopyrite semiconductor $ZnSnP_2$, which lacks inversion symmetry, and calculate the shift-current conductivity. We find that the magnitude of the shift current is comparable to the recently measured values on other ferroelectric semiconductors and an order of magnitude larger than bismuth ferrite. The peak response for both optical and shift-current conductivity, which mainly comes from P-3p and Sn-5p orbitals, is several eV above the band gap.

DOI: 10.1103/PhysRevMaterials.4.064602

I. INTRODUCTION

Ternary compounds $A^{II}B^{IV}C_2^V$ and $A^IB^{III}C_2^{VI}$ (where A,B = metals, C = sulfur/nitrogen family) having a chalcopyrite structure are of considerable interest because of their structural, mechanical, thermoelectric, and nonlinear optical properties [1]. They are also promising materials for spintronics application because of the ability to host ferromagnetism at room temperature [2,3]. The chalcopyrite structures are derived from the binary analogs $M^{III}C^V$ and $M^{II}C^{VI}$ in cubic zinc-blende structures by doubling the unit cell along c, leading to a body-centered-tetragonal unit cell. Each cation (anion) is surrounded by four nearest-neighbor anions (cations) as in the zinc-blende structure. The A and B cations alternatively occupy the Zn positions and form a tetrahedral bonding of the two cation sublattices. The reduced symmetry lowers the band gap significantly in the ternary compounds compared to their binary analogs [4]. This spatial symmetry reduction also plays an important role to realize the topological insulating and Weyl semimetallic phases in some ternary chalcopyrites [5–13].

Of particular interest is the ternary compound $ZnSnP_2$ (ZSP), type $A^{II}B^{IV}C_2^V$, which is now recognized as an alternative photoabsorber material in solar cell applications [14,15]. It undergoes a structural transition from the ordered chalcopyrite $ZnSnP_2$ (CH-ZSP) structure to a disordered sphalerite structure (SP-ZSP) at 990 K [16]. In SP-ZSP, the Sn and Zn atoms are randomly distributed over the cation sublattice. In comparison, in the ordered CH-ZSP, the P^{3-} anions are surrounded by two Zn^{2+} (A-type) and two Sn^{4+} (B-type) cations, while each cation is surrounded by four anions. Due to the possibility of band-gap engineering and tunability of the electronic and optical properties, the electronic structure and properties of ZSP are being investigated both theoretically and experimentally [14,17–22]. In comparison to other well-known chalcopyrite ternary compounds, an important feature of CH-ZSP is that the ground state is a trivial insulator, but lacks inversion symmetry due to the displacement of the anion positions (anion shift) towards one of the cations as compared to the ideal case obtained by doubling the cubic zinc-blende unit cell (see Sec. III for details). It is also anisotropic due to the presence of two types of cationic bonding which also gives rise to high birefringence.

An interesting and potentially useful property of noncentrosymmetric crystals is that in such materials, symmetry allows incident photons to induce a photocurrent. This is a bulk photovoltaic phenomenon and the induced current is referred to as the shift current [23–28]. In contrast to a conventional drift photocurrent under an electric field, the shift current originates from the charge center shifts in real space due to a difference in the Berry connection between the valence and conduction bands involved in the optical excitation process [24,28]. Recently, Weyl semimetals (WSMs) have been theoretically investigated for such nonlinear optical phenomena [27,29–35].

The shift current with a less dissipative character has remarkable advantages over the conventional drift photocurrent driven by a built-in potential or external electric field [36–38]. For example, it depends on the polarization direction of the incident photon field, is insensitive to the sample resistivity or barrier formation near the electrodes [39], and is also independent of the external bias voltage [40,41].

Moreover, photocurrents induced by optical transitions obeying dipole and polarization selection rules naturally permit ultrafast manipulation. In particular, shift currents induced by properly tuned external pulsed photon sources can create

*b.sadhukhan@ifw-dresden.de

†r.ray@ifw-dresden.de

coherent electromagnetic wave emission in the terahertz frequency regime, where control of the ellipticity and chirality over a broad spectral range is notoriously difficult [42,43].

Here we show, using a recently developed multiband approach [27], that the shift-current conductivity [27,44,45] in CH-ZSP is comparable to that in SbSI [46], and an order of magnitude larger than the famous multiferroic $BiFeO_3$ [47]. The multiband approach involves the full set of Bloch states and a sum over all intermediate states participating in three-band transitions is considered. The three-band virtual transitions make the dominant contributions and are distributed uniformly in the momentum space. Naturally, in comparison to the widely used two-band effective models, estimates based on the multiband approach are accurate and highly desirable for materials application.

A key challenge in an accurate density functional theory (DFT)-based description of insulating materials is the well-known problem of band-gap underestimation by the local and semilocal functionals. These problems can be cured by employing schemes which take into account the self-energy of a many-body electronic system, such as the GW approximation [48] and the hybrid exchange correlation (HSE) functional [49]. However, they are computationally very expensive. At the same time, while the HSE functionals improve the band gap close to the experimental value, it may overestimate the lattice constants and the atomic displacement associated with structural distortion, which may eventually lead to an inaccurate estimate of material properties. For example, in the noncentrosymmetric compound $BaTiO_3$, such overestimation affects the ferroelectricity and gives an inaccurate optical response [50–52].

Traditionally, the deficiency associated with the band gap is addressed by using a simple "scissors operation" [53,54] on the standard DFT [using generalized gradient approximation/local density approximation (GGA/LDA)] bands, whereby the conduction bands are rigidly shifted such that the resulting electronic band gap matches the experimental value. Within this procedure, the optical response obtained within LDA/GGA is shifted by the same amount (referred to as scissor shift in the following) and retains the features obtained from standard DFT [55]. As an alternative, a semiempirical DFT + U approximation might be used to improve the band-gap values. Very recently, an empirical Tran-Blaha modified Becke-Johnson (TB-mBJ) potential [56] was shown to lead to an accuracy that is comparable to the very expensive hybrid functional and GW approximation at a computational cost comparable to standard DFT calculations. Here, we thus consider the latter three approaches, viz., the scissors operation (GGA + Δ), DFT + U, and TB-mBJ methods, and discuss their implications for the electronic and optical properties of CH-ZSP.

II. COMPUTATIONAL DETAILS

We performed density functional theory (DFT) calculations within the Perdew-Burke-Ernzerhof (PBE) implementation [57] of the GGA functional using the full-potential local-orbital (FPLO) code [58,59]. Self-consistent calculations employing the default scalar relativistic approximation were performed on a k mesh with 18 × 18 × 18 subdivisions. Starting from the experimental structure [60], several crystal structures with different unit-cell volumes V were considered: $0.90V_{\rm exp} \leqslant V \leqslant 1.10V_{\rm exp}$, where $V_{\rm exp}$ is the unit-cell volume of the experimental crystal structure. For each case, the internal parameters (atomic positions) were optimized such that the net force on each atom was less than 1 meV/Å and the ground-state energy was evaluated. The optimized structure was considered for further detailed study of the electronic and optical properties. The spin-orbit effects are expected to be small and were, therefore, not considered (see the Appendix).

To overcome the issue of band-gap underestimation, both DFT + U and TB-mBJ calculations were carried out. The on-site orbital-dependent electron-electron correlations (U) were applied to Zn-3d as well as P-3p states, and the evolution of the band gap was studied.

The TB-mBJ calculations [56] were carried out using the full-potential augmented plane waves + local orbital (APW + lo) method as implemented in the WIEN2K code [61]. A good quantitative and qualitative agreement between the two codes was obtained within the scalar relativistic GGA calculations. For the TB-mBJ potential, the self-consistent c parameter was used [56]. The energy convergence of the obtained solutions is better than 10^{-5} Ryd per unit cell and the charge convergence is better than $10^{-4}\,e$/a.u.^{3}.

The optical properties within the linear response theory were obtained using the well-known relations: the imaginary part of the dielectric function is given by

$$\epsilon_2^{\alpha\beta}(\omega) = \mathrm{Im}[\epsilon_{\alpha\beta}(\omega)] = -\frac{4\pi^2 e^2}{m_0^2\omega^2}\int d\mathbf{k}\sum_{n,l}(f_n - f_l) \times \frac{\langle \mathbf{k}n|\hat{v}_\alpha|\mathbf{k}l\rangle\langle \mathbf{k}l|\hat{v}_\beta|\mathbf{k}n\rangle}{(E_{\mathbf{k}n} - E_{\mathbf{k}l} - \hbar\omega - i\delta)}, \quad (1)$$

where, $\alpha, \beta = (x, y, z)$ are the Cartesian coordinates, $\hat{v}_\alpha = \hat{p}_\alpha/m_0$ is the velocity operator along α, m_0 is the free electron mass, $|\mathbf{k}n\rangle$ are the wave functions corresponding to the band with energy $E_{\mathbf{k}n}$ at momentum $\mathbf{k}$ and index n, $f_n \equiv f(E_{\mathbf{k}n})$ is the Fermi function for the state with energy $E_{\mathbf{k}n}$, and $\hbar\omega$ is the incident photon energy. $\delta = \hbar/\tau_s$ is the broadening parameter which depends inversely on the single-particle relaxation time associated with the quantum mechanical broadening τ_s. The real part can be obtained via the Kramer-Kronig relation,

$$\epsilon_1^{\alpha\beta}(\omega) = \mathrm{Re}[\epsilon_{\alpha\beta}(\omega)] = \delta_{\alpha\beta} + \frac{1}{\pi}\mathcal{P}\int_{-\infty}^{\infty} d\omega' \frac{\mathrm{Im}[\epsilon_{\alpha\beta}(\omega')]}{\omega - \omega'}. \quad (2)$$

All optical response functions can now be derived from these. In particular, the optical conductivity is

$$\sigma_{\alpha\beta}(\omega) = \frac{\omega\epsilon_2^{\alpha\beta}(\omega)}{4\pi}. \quad (3)$$

To calculate the shift-current response, we used the general relation for the photoconductivity in quadratic response theory

[27,44,45],

$$\sigma^{\gamma}_{\alpha\beta} = \frac{|e|^3}{8\pi^3\omega^2}\mathrm{Re}\left\{\phi_{\alpha\beta}\sum_{\Omega=\pm\omega}\sum_{l,m,n}\int_{BZ} d\mathbf{k}(f_l - f_n) \times \frac{\langle \mathbf{k}n|\hat{v}_\alpha|\mathbf{k}l\rangle\langle \mathbf{k}l|\hat{v}_\beta|\mathbf{k}m\rangle\langle \mathbf{k}m|\hat{v}_\gamma|\mathbf{k}n\rangle}{(E_{\mathbf{k}n} - E_{\mathbf{k}m} - i\delta)(E_{\mathbf{k}n} - E_{\mathbf{k}l} + \hbar\Omega - i\delta)}\right\}. \quad (4)$$

The conductivity $\sigma^{\gamma}_{\alpha\beta}$ ($\alpha, \beta, \gamma = x, y, z$) is a third-rank tensor representing the photocurrent J_γ generated by an electrical field via $J_\gamma = \sigma^{\gamma}_{\alpha\beta}\mathcal{E}^*_\alpha\mathcal{E}_\beta$. $\phi_{\alpha\beta}$ is the phase difference between the driving fields $\mathcal{E}_\alpha$ and $\mathcal{E}_\beta$. The real part of the integral in Eq. (4) describes the shift-current response under a linearly polarized light. Note that while the above equation does not explicitly reflect the topological nature of the shift current, it depends on the topological Berry connection and Berry curvature [24,27,41].

The starting point for the shift-current calculation is a band structure and the corresponding eigenstates and energies in the Brillouin zone. To this end, a tight-binding model was obtained using maximally projected Wannier functions (WFs) for the Zn-3d, Sn-4d, 5s, 5p, and P-3p orbitals in the energy range of -7.0 to 5.0 eV. The typical mismatch between the tight-binding model derived from such Wannier functions and the self-consistent DFT band structure was $\lesssim 1$ meV. For the integral in Eq. (4), the Brillouin zone (BZ) was sampled by a $200 \times 200 \times 200$ k mesh with satisfactory convergence. The value of the conductivity changes by less than 3–4% above that k mesh. A typical value of the broadening parameter was used for both the linear and nonlinear response: in ordinary metals and semiconductors, the ratio of the transport relaxation time (τ_t) and the single-particle relaxation time associated with the quantum mechanical broadening (τ_s) is $\tau_t/\tau_s = 1$ [62–65]. In semiconductors, the transport relaxation time $\tau_t \approx$ femtoseconds (10^{-15} sec) at room temperature [66,67], leading to $\delta \approx \hbar/\tau_s = 0.1$ at room temperature.

$ZnSnP_2$ belongs to the D_{2d} (-4m2) point group in the ferroelectric phase. Therefore, it has the second-order photoconductivity ($\sigma^{\gamma}_{\alpha\beta}$) tensor of the form

$$\sigma^{\gamma}_{\alpha\beta} = \begin{pmatrix} 0 & 0 & 0 & \sigma^x_{yz} & 0 & 0 \\ 0 & 0 & 0 & 0 & \sigma^y_{xz} & 0 \\ 0 & 0 & 0 & 0 & 0 & \sigma^z_{xy} \end{pmatrix}.$$

The second-harmonic susceptibility $\chi^{\gamma}_{\alpha\beta}$ ($\chi^{\gamma}_{\alpha\beta} = \sigma^{\gamma}_{\alpha\beta}/2i\omega\epsilon$) is governed by the same symmetry and, therefore, has similar form. The crystal has a mirror reflection M_{xy} in the x-y plane, which exchanges the x and y indexes. In addition, the 4_2 screw rotation symmetry about the z axis gives $\sigma^x_{yz} = \sigma^y_{xz}$, leaving only two independent nonlinear optical photoconductivity tensor elements σ^x_{yz} and σ^z_{xy}.

III. RESULTS AND DISCUSSION

Ternary ZSP crystallizes in a body-centered-tetragonal structure which in the chalcopyrite phase (CH-ZSP) has the space group $I\bar{4}2d$ (No. 122). It has eight atoms per primitive unit cell. Basically, it is a superlattice of a zinc-blende structure obtained by doubling the zinc-blende unit cell along the z direction. The unit cell of $ZnSnP_2$ is shown in Fig. 1(a). In an ideal zinc-blende structure of a binary compound, each anion has four similar cations as nearest neighbors. So, all four bond lengths are equal and the charge distribution is identical around each bond. Consequently, in a binary compound with a zinc-blende structure, u is 0.25 and $\eta = c/a = 1$. Therefore, the ideal case for the doubled unit cell corresponds to $u = 0.25$ and $\eta = c/a = 2$.

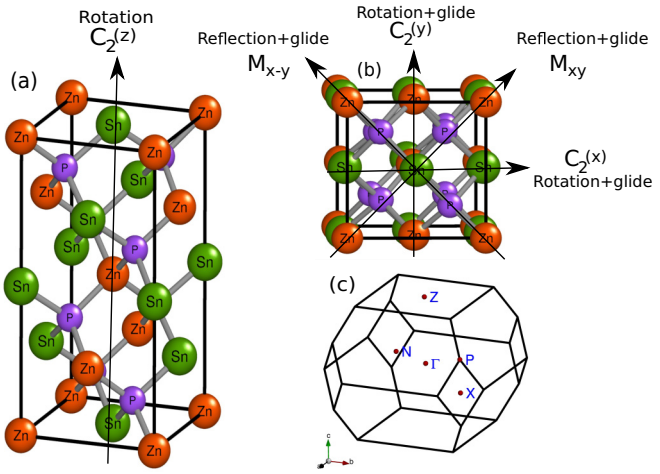

FIG. 1. Unit cell of the chalcopyrite $ZnSnP_2$ (CH-ZSP) lattice: (a) side view and (b) top view. It has two twofold glide rotational and mirror symmetries $C_2(x)$, $C_2(y)$, M_{xy}, and M_{x-y}. (c) Brillouin zone (BZ) along with the high-symmetric points.

In CH-ZSP, each anion has two Zn and two Sn cations as nearest neighbor. Due to dissimilar atoms as neighbors, the anion acquires an equilibrium position closer to one pair of cation than to the other. The displacement of the position of the anion thus leads to bond alternation. In the most general case, $u \neq 0.25$ and $\eta \neq 2$. In contrast to other chalcopyrite compounds, CH-ZSP lacks tetragonal distortion ($\eta = 2$) but exhibits displacement of anions towards the smaller cation (anion shift). The positions of the different types of atoms in the tetragonal unit cell are the Zn atom at (0, 0, 0), Sn atom at (0, 0, 0.5), and P atom at (u, 0.25, 0.125), where u is the anion displacement parameter. The equilibrium lattice parameters and the optimal internal parameters for CH-ZSP, along with the corresponding experimental values, are presented in Table I. Compared to the binary compound, the cubic symmetry is broken and the noncentrosymmetric CH-ZSP crystal has two twofold glide rotational symmetries $C_2(x)$, $C_2(y)$, and two glide mirror symmetries M_{xy} and M_{x-y}. It also has a twofold rotational symmetry along z (see Fig. 1).

The band structure along the high-symmetry lines in the Brillouin zone and the density of states (DOS) is shown in Fig. 2. A direct band gap is found at the Γ point [see Fig. 2(a)].

TABLE I. The experimental and equilibrium structural parameters for CH-ZSP. Please see text for details. The experimental parameters were taken from Ref. [60].

$ZnSnP_2$	a (Å)	c (Å)	u
Experimental	5.7382	11.4764	0.239
Theoretical	5.7382	11.4764	0.2272

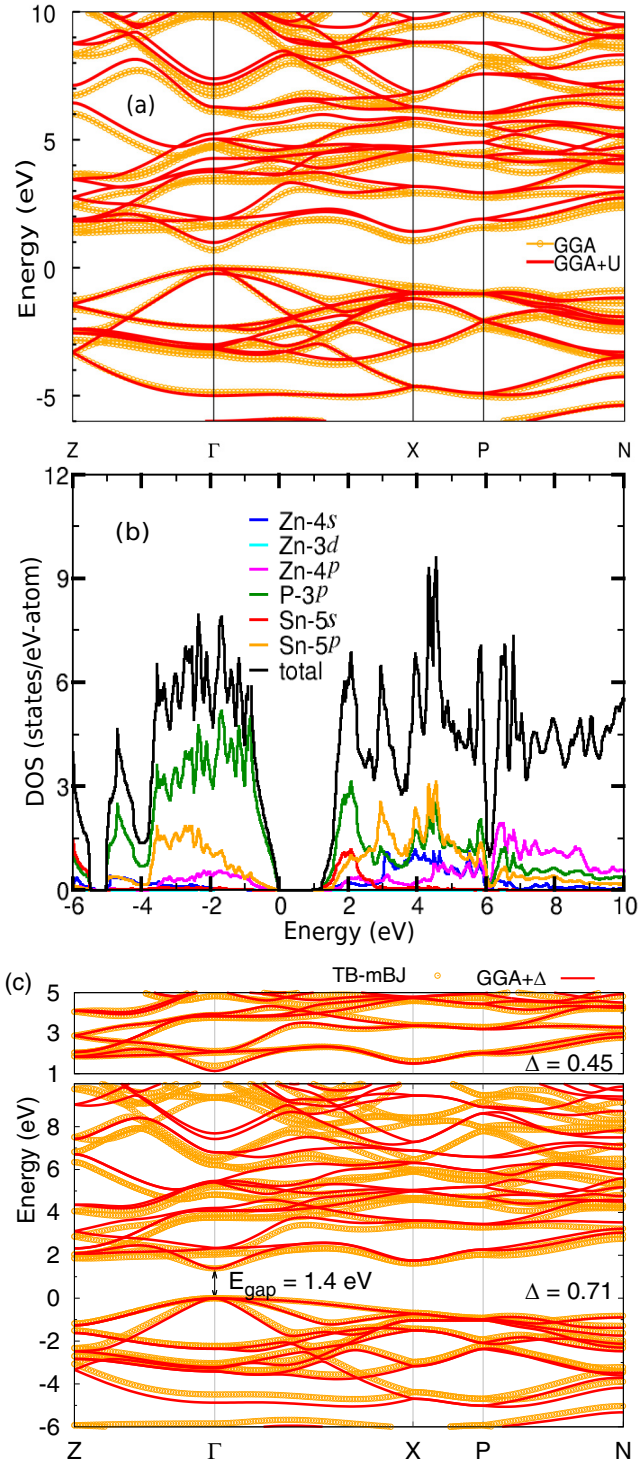

FIG. 2. (a) The band structure from GGA and GGA + U, showing a direct band gap at Γ. The GGA band gap is ∼0.69 eV, whereas the GGA + U band gap is ∼1.05 eV, obtained with $U_d = 10$ eV and $U_p = 2$ eV (see text for details). (b) The total and partial density of states within GGA + U. (c) Comparison of band structures obtained within GGA + Δ and TB-mBJ calculations. For comparison, the GGA conduction bands have been scissor shifted by Δ = 0.71 eV (bottom panel) to match the band gap, and Δ = 0.45 eV in an energy range of 1 and 5 eV (top panel), showing the qualitative and quantitative agreement between the two methods in the description of the conduction-band states.

Within GGA, the band gap is ∼0.69 eV, in good agreement with earlier calculations [21]. This is, however, merely ∼41% of the experimental gap of 1.68 eV [18], implying that a scissor shift of Δ ∼ 1 eV should be applied to obtain a quantitative agreement with the experimental results.

Within the +U scheme, the band gap can reach 1.05 eV upon adjusting the U parameter. Since the dominant contribution across the Fermi energy is due to P-3p states [see Fig. 2(b), and discussed below], one also needs to consider U_p for these states along with U_d for Zn-3d states. The largest band gap is obtained for $U_d = 10$ eV and $U_p = 2$ eV. In this context, it should be noted that the application of U-term correlations simultaneously to cation d and anion p states is not unprecedented, the most relevant example being ZnO [68,69]. At the same time, a similar large value of $U_d = 10$ eV was also suggested in Ref. [70].

The atomic contributions to DOS across the Fermi energy within GGA + U remain remarkably similar to the GGA results, and are shown in Fig. 2(b). The valence-band region up to −5 eV is mainly composed of p states, with a dominant contribution by P-3p, followed by Sn-5p and Zn-4p. The valence-band maximum is composed primarily of the P-3p states, and the Zn-4s states lie relatively deep in the valence band, between −4 and −5 eV. On the other hand, the conduction-band region is contributed by the P-3p, Sn-5s, and 5p states, reflecting strong covalency effects in CH-ZSP [see Fig. 2(b)].

The most notable difference between GGA and GGA + U is the relative position and spread of the Zn-3d states. Arguably, the Zn-3d states within GGA are overhybridized with the Zn-4p states similar to other strongly covalent systems involving Zn [69]. As a result, they are underbound and lie somewhat higher in the energy, in the range of −5.1 to −7.6 eV, (just) below the P-4p states in the valence band. This, in turn, leads to severe underestimation of the band gap within GGA [68,69]. The location of the Zn-3d states can, in principle, be tuned within the GGA + U functional. Within +U, they shift somewhat lower in energy and are more localized (smaller bandwidth), leading to a well-defined gap in the DOS at ∼ − 5 eV. This is accompanied by redistribution of the Zn-4s and Zn-4p contributions. Eventually, the +U method improves the band gap over GGA, but is not sufficient.

On the other hand, application of the TB-mBJ potential leads to a gap of ∼1.4 eV [see Fig. 2(c)], in good agreement with the previously reported value [21]. This is a significant improvement over the GGA and GGA + U values; however, it remains at only ∼83% of the experimentally reported value. This is not surprising since P-3p states contribute significantly to the states across the Fermi energy [71]. Such a discrepancy is indicative of the fact that many-body effects could be important for CH-ZSP and that an approach accounting for such many-body effects, such as DFT calculations with hybrid functional or GW approximation, may be required to address the full band-gap issue here.

To compare the TB-mBJ band structure with that of GGA, a scissor shift Δ = 0.71 eV is required, as shown in the lower panel of Fig. 2(c). However, a somewhat smaller scissor shift of Δ = 0.45 shows a remarkably good qualitative and quantitative agreement between the two methods [see the top panel in Fig. 2(c)]. A comparison of the atom-resolved DOS

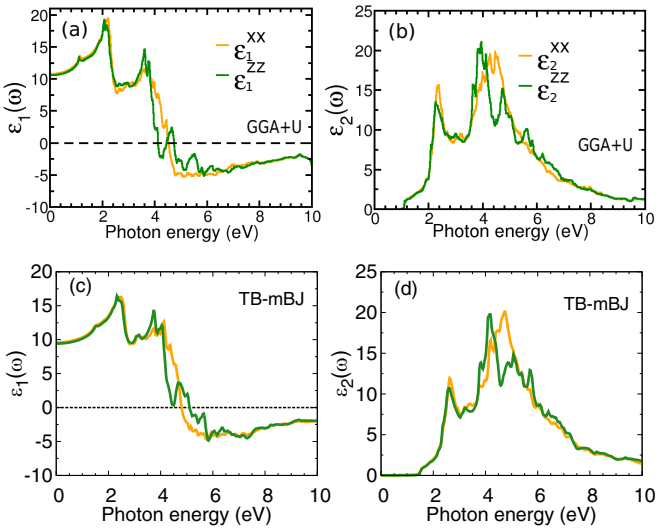

FIG. 3. The real and imaginary parts of the dielectric constant as a function of the incident photon energy obtained within the (a),(b) GGA + U and (c),(d) TB-mBJ scheme, showing overall agreement.

(not shown) suggests that the relative compositions of the conduction bands are similar in both approaches. Therefore, within all the considered approaches, the valence-band edge remains largely unaffected, while the qualitative description of the conduction bands and their composition is nearly the same.

To summarize, within the considered methods, the description of CH-ZSP predominantly differs only in the predicted value of the band gap. Therefore, different values of scissor shift are required to compare the GGA results with the others. A large value of $\Delta \sim 1$ eV is needed to match with the experimental results, whereas $\Delta = 0.36$ eV and $\Delta = 0.71$ eV is needed to compare with the GGA + U and the TB-mBJ results, respectively.

To further ascertain the degree of agreement between the considered methods, we also compare the linear optical response. Figure 3 shows the real and imaginary part of the dielectric function obtained within GGA + U and its comparison with the corresponding results from TB-mBJ. Tetragonal symmetry of the crystal structure implies that the in-plane ($\alpha\beta = xx, yy$) and the out-of-plane ($\alpha\beta = zz$) components are distinct. The qualitative similarities in both the schemes is evident. Within GGA + U, the real part of the dielectric constant ϵ_1 has prominent peaks at approximately 2 and 3.7 eV, and the zero-energy crossings lie between 4.5 and 5 eV. The imaginary part of the dielectric constant ϵ_2 is also characterized by two prominent peaks, at ∼2 eV and between 4.0 and 4.5 eV, similar to ϵ_1. These peak positions correspond to the interband transitions between the valence- and conduction-band states. The dominant peak in ϵ_2^{zz} (at ∼4 eV) lies slightly lower than in ϵ_2^{xx}, as expected from the respective zero-energy crossings in ϵ_1. Considering a scissor shift of $\Delta \sim 0.35$, required to match the band gaps between the GGA + U and TB-mBJ methods, the peak position in ϵ_1 and ϵ_2, as well the zero-energy crossing in ϵ_1 are in good agreement within the two approaches.

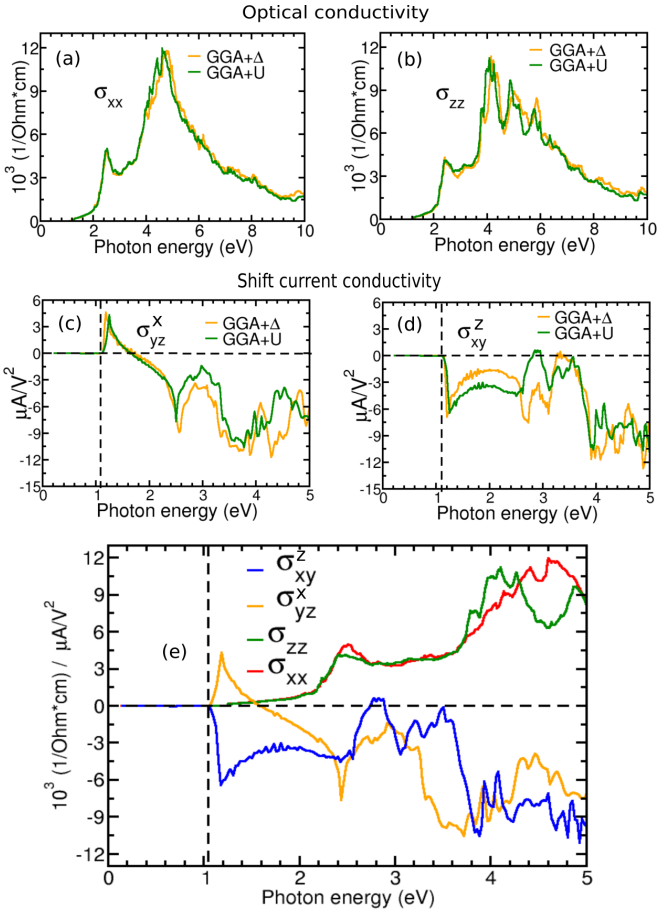

FIG. 4. The optical conductivity (a) σ_{xx} and (b) σ_{zz} from GGA + U and GGA + Δ ($\Delta = 0.36$ eV). The shift-current conductivity (c) σ^x_{yz} and (d) σ^z_{xy} from GGA + U and GGA + Δ. (e) Both the optical and shift-current conductivity from GGA + U are plotted on the same scale.

The zero-frequency limit of $\epsilon_1(\omega)$, $\epsilon_1(0)$, is an important quantity. It represents the electronic part of the static dielectric constant and depends strongly on the band gap. The static dielectric constant is found to be $\epsilon_1(0) = 10.56$ eV within GGA + U. In comparison, this value was measured to be 10 eV [72,73], while the TB-mBJ calculations yield 9.7.

As the nonlinear optical properties crucially depend on the wave functions [44], reliable estimates of the optical properties, especially the magnitude of the shift current, can thus be obtained even within the scissors operator method GGA + Δ. Therefore, in the following, we focus on the GGA + Δ and GGA + U methods with the understanding that an additional scissor shift of ∼0.6 eV (∼0.4 eV) may be required for a quantitative comparison with experiments (TB-mBJ).

Figure 4 shows the calculated optical and shift-current conductivity for CH-ZSP. The obtained GGA response has been scissor shifted by $\Delta = 0.36$ eV to compare with GGA + U. The structure and magnitude of the optical response do not depend too much on GGA + U. We begin with a comparison of the optical conductivity obtained within GGA and GGA + U, shown in Figs. 4(a) and 4(b), respectively, for σ_{xx} and σ_{zz}. The optical conductivities are in very good agreement, as expected from the fact that both of these methods provide a

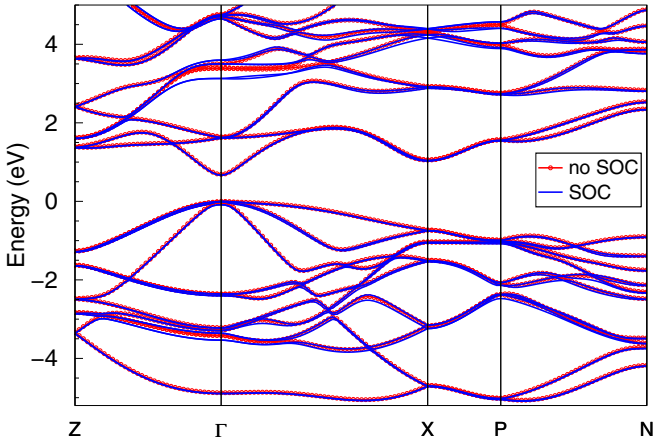

FIG. 5. A comparison of the scalar relativistic (no SOC) and full relativistic (SOC) band structures for $ZnSnP_2$.

qualitatively similar description of the conduction and valence bands. The main optical conductivity peak in σ_{xx} appears at 4.61 eV, with a low-energy peak at 2.52 eV, and for σ_{zz}, the peak appears at 4.08 and 2.43 eV, respectively. These peak positions are consistent with the corresponding peak positions in the imaginary part of the dielectric function ϵ_2.

In the shift-current conductivity [see Figs. 4(c)–4(e)], σ^x_{yz} and σ^z_{xy} are the only nonvanishing, independent components of the third-rank tensor $\sigma^\gamma_{\alpha\beta}$. Similar to the optical conductivity, the shift-current response starts only above the band gap. Interestingly, the shift current shows a strong increase at the gap edge, in contrast to the optical current conductivity, which increases slowly above the gap. Figures 4(c) and 4(d) show the calculated shift current for the σ^x_{yz} and σ^z_{xy} components. The shift-current response for both xy and yz polarized light is negative, though σ^x_{yz} has a small positive contribution near the band gap. The shift-current conductivity is around 6 $\mu A/V^2$ near the band gap for both σ^x_{yz} and σ^z_{xy}, which is comparable to recent experimental observations on the semiconductor SbSI [46], and an order of magnitude larger than the famous multiferroelectric compound bismuth ferrite (0.5 $\mu A/V^2$) [47]. Similar to the optical conductivity discussed before, the shift current exhibits a large increase to 12 $\mu A/V^2$ at photon energy at ∼3.5–4 eV. This is due to the large real-space charge center shift between valence electrons and conduction electrons, which contributes mainly from $3p$ orbitals of P atoms to $5p$ orbitals of Sn atoms.

IV. CONCLUSION AND OUTLOOK

In conclusion, we investigated the nonlinear photocurrent in the noncentrosymmetric chalcopyrite semiconductor $ZnSnP_2$ based on first-principles calculations. Based on a detailed analysis of the electronic properties of CH-ZSP within the traditional scissors operator method GGA + Δ, GGA + U, and TB-mBJ methods, we find that TB-mBJ leads to a much better agreement (∼83%) with the reported experimental band gap. More importantly, although various methods rely on different approaches, the description of the electronic bands within all of these methods is remarkably similar. This bodes well for the reliability of our estimates for linear and nonlinear optical properties based on either of the methods. The shift-current conductivity that we find is around 6 $\mu A/V^2$ near the band gap and 12 $\mu A/V^2$ at photon energy 3.5–4 eV. This comes mainly from the large real-space charge center shift between valence electrons and conduction electrons of P-$3p$ and Sn-$5p$ orbitals. Distinct from the diffusion mechanism in the p-n junction-based photogalvanic effect, the generation of photocurrent under linear polarized electromagnetic radiation in $ZnSnP_2$ is dominated by a Berry-phase-related shift current. Due to the underlying selection rules, ultrafast photoinduced currents will strongly depend on the crystal orientation and laser polarization. This can offer a promising avenue to achieve efficient generation and control of secondary terahertz radiation, which in $ZnSnP_2$ will result from the intrinsic shift-current mechanism [43]: the magnitude of the shift current is comparable to the recent experimental value on SbSI [46] and an order of magnitude larger than the multiferroelectric compound bismuth ferrite (0.5 $\mu A/V^2$) [47].

ACKNOWLEDGMENTS

We thank Manuel Richter for helpful discussions and Ulrike Nitzsche for technical assistance. This work was supported by the German Research Foundation (DFG) via Grant No. SFB 1143, Project No. A5 and by the Würzburg-Dresden Cluster of Excellence on Complexity and Topology in Quantum Matter — *ct.qmat* (EXC 2147, Project No. 39085490).

APPENDIX: ROLE OF SPIN-ORBIT COUPLING (SOC)

Figure 5 shows a comparison of the band structures of CH-ZSP within the scalar relativistic ("no SOC") and full relativistic GGA calculations. Sizable differences are found only around −3 eV and 3.5 eV, where the Sn-$5p$ contribution is dominant (see Fig. 2).

[1] M. C. Ohmer and R. Pandey, MRS Bull. **23**, 16 (1998).
[2] G. A. Medvedkin, T. Ishibashi, T. Nishi, K. Hayata, Y. Hasegawa, and K. Sato, Jpn. J. Appl. Phys. **39**, L949 (2000).
[3] S. Cho, S. Choi, G.-B. Cha, S. C. Hong, Y. Kim, Y.-J. Zhao, A. J. Freeman, J. B. Ketterson, B. J. Kim, Y. C. Kim *et al.*, Phys. Rev. Lett. **88**, 257203 (2002).
[4] C.-Y. Yeh, S.-H. Wei, and A. Zunger, Phys. Rev. B **50**, 2715 (1994).
[5] W. Feng, D. Xiao, J. Ding, and Y. Yao, Phys. Rev. Lett. **106**, 016402 (2011).
[6] J. Ruan, S.-K. Jian, D. Zhang, H. Yao, H. Zhang, S.-C. Zhang, and D. Xing, Phys. Rev. Lett. **116**, 226801 (2016).

[7] R. Juneja, R. Shinde, and A. K. Singh, J. Phys. Chem. Lett. **9**, 2202 (2018).
[8] A. Lau and C. Ortix, Phys. Rev. Lett. **122**, 186801 (2019).
[9] L. Fu and C. L. Kane, Phys. Rev. B **76**, 045302 (2007).
[10] B. A. Bernevig, T. L. Hughes, and S.-C. Zhang, Science **314**, 1757 (2006).
[11] D. Xiao, Y. Yao, W. Feng, J. Wen, W. Zhu, X.-Q. Chen, G. M. Stocks, and Z. Zhang, Phys. Rev. Lett. **105**, 096404 (2010).
[12] S. Chadov, X. Qi, J. Kübler, G. H. Fecher, C. Felser, and S.-C. Zhang, Nat. Mater. **9**, 541 (2010).
[13] H. Lin, L. A. Wray, Y. Xia, S. Xu, S. Jia, R. J. Cava, A. Bansil, and M. Z. Hasan, Nat. Mater. **9**, 546 (2010).
[14] D. O. Scanlon and A. Walsh, Appl. Phys. Lett. **100**, 251911 (2012).
[15] Y. Kumagai, M. Choi, Y. Nose, and F. Oba, Phys. Rev. B **90**, 125202 (2014).
[16] J. L. Shay and J. H. Wernick, *Ternary Chalcopyrite Semiconductors: Growth, Electronic Properties, and Applications*, International Series of Monographs in the Science of the Solid State Vol. 7 (Elsevier, San Diego, CA, USA, 2017).
[17] K. Nakatani, T. Minemura, K. Miyauchi, K. Fukabori, H. Nakanishi, M. Sugiyama, and S. Shirakata, Jpn. J. Appl. Phys. **47**, 5342 (2008).
[18] P. St-Jean, G. Seryogin, and S. Francoeur, Appl. Phys. Lett. **96**, 231913 (2010).
[19] S. Mishra and B. Ganguli, J. Solid State Chem. **200**, 279 (2013).
[20] S. Sahin, Y. Ciftci, K. Colakoglu, and N. Korozlu, J. Alloys Compd. **529**, 1 (2012).
[21] Y. Xu, Z. M. Ao, D. F. Zou, G. Z. Nie, W. Sheng, and D. W. Yuan, Phys. Lett. A **379**, 427 (2015).
[22] S. Mukherjee, T. Maitra, A. Nayak, A. Pradhan, M. Mukhopadhyay, B. Satpati, and S. Bhunia, Mater. Chem. Phys. **204**, 147 (2018).
[23] J. E. Sipe and A. I. Shkrebtii, Phys. Rev. B **61**, 5337 (2000).
[24] T. Morimoto and N. Nagaosa, Phys. Rev. B **94**, 035117 (2016).
[25] F. Nastos and J. E. Sipe, Phys. Rev. B **74**, 035201 (2006).
[26] F. Nastos and J. E. Sipe, Phys. Rev. B **82**, 235204 (2010).
[27] Y. Zhang, H. Ishizuka, J. van den Brink, C. Felser, B. Yan, and N. Nagaosa, Phys. Rev. B **97**, 241118(R) (2018).
[28] T. Morimoto and N. Nagaosa, Sci. Adv. **2**, e1501524 (2016).
[29] P. Goswami, G. Sharma, and S. Tewari, Phys. Rev. B **92**, 161110(R) (2015).
[30] H. Ishizuka, T. Hayata, M. Ueda, and N. Nagaosa, Phys. Rev. Lett. **117**, 216601 (2016).
[31] I. Sodemann and L. Fu, Phys. Rev. Lett. **115**, 216806 (2015).
[32] T. Morimoto, S. Zhong, J. Orenstein, and J. E. Moore, Phys. Rev. B **94**, 245121 (2016).
[33] E. J. König, H.-Y. Xie, D. A. Pesin, and A. Levchenko, Phys. Rev. B **96**, 075123 (2017).
[34] Y. Zhang, Y. Sun, and B. Yan, Phys. Rev. B **97**, 041101(R) (2018).
[35] X. Yang, K. Burch, and Y. Ran, arXiv:1712.09363.
[36] T. Choi, S. Lee, Y. J. Choi, V. Kiryukhin, and S.-W. Cheong, Science **324**, 63 (2009).
[37] S. Yang, J. Seidel, S. Byrnes, P. Shafer, C.-H. Yang, M. Rossell, P. Yu, Y.-H. Chu, J. Scott, J. Ager *et al.*, Nat. Nanotechnol. **5**, 143 (2010).
[38] I. Grinberg, D. V. West, M. Torres, G. Gou, D. M. Stein, L. Wu, G. Chen, E. M. Gallo, A. R. Akbashev, P. K. Davies *et al.*, Nature (London) **503**, 509 (2013).
[39] N. Ogawa, M. Sotome, Y. Kaneko, M. Ogino, and Y. Tokura, Phys. Rev. B **96**, 241203(R) (2017).
[40] L. Z. Tan, F. Zheng, S. M. Young, F. Wang, S. Liu, and A. M. Rappe, Npj Comput. Mater. **2**, 1 (2016).
[41] S. M. Young and A. M. Rappe, Phys. Rev. Lett. **109**, 116601 (2012).
[42] N. Amer, W. C. Hurlbut, B. Norton, Y.-S. Lee, and T. Norris, Appl. Phys. Lett. **87**, 221111 (2005).
[43] Y. Gao, S. Kaushik, E. Philip, Z. Li, Y. Qin, Y. Liu, W. Zhang, Y. Su, X. Chen, H. Weng *et al.*, Nat. Commun. **11**, 720 (2020).
[44] R. von Baltz and W. Kraut, Phys. Rev. B **23**, 5590 (1981).
[45] W. Kraut and R. von Baltz, Phys. Rev. B **19**, 1548 (1979).
[46] M. Sotome, M. Nakamura, J. Fujioka, M. Ogino, Y. Kaneko, T. Morimoto, Y. Zhang, M. Kawasaki, N. Nagaosa, Y. Tokura *et al.*, Proc. Natl. Acad. Sci. USA **116**, 1929 (2019).
[47] S. M. Young, F. Zheng, and A. M. Rappe, Phys. Rev. Lett. **109**, 236601 (2012).
[48] F. Aryasetiawan and O. Gunnarsson, Rep. Prog. Phys. **61**, 237 (1998).
[49] J. Heyd, G. E. Scuseria, and M. Ernzerhof, J. Chem. Phys. **118**, 8207 (2003).
[50] S. Sanna, C. Thierfelder, S. Wippermann, T. P. Sinha, and W. G. Schmidt, Phys. Rev. B **83**, 054112 (2011).
[51] G. Gupta, T. Nautiyal, and S. Auluck, Phys. Rev. B **69**, 052101 (2004).
[52] D. Bagayoko, G. Zhao, J. Fan, and J. Wang, J. Phys.: Condens. Matter **10**, 5645 (1998).
[53] R. W. Godby, M. Schlüter, and L. J. Sham, Phys. Rev. B **37**, 10159 (1988).
[54] Z. H. Levine and D. C. Allan, Phys. Rev. Lett. **63**, 1719 (1989).
[55] F. Nastos, B. Olejnik, K. Schwarz, and J. E. Sipe, Phys. Rev. B **72**, 045223 (2005).
[56] F. Tran and P. Blaha, Phys. Rev. Lett. **102**, 226401 (2009).
[57] J. P. Perdew, K. Burke, and M. Ernzerhof, Phys. Rev. Lett. **77**, 3865 (1996).
[58] K. Koepernik and H. Eschrig, Phys. Rev. B **59**, 1743 (1999).
[59] https://www.fplo.de.
[60] A. Vaipolin, N. Goryunova, L. Kleshchinskii, G. Loshakova, and E. Osmanov, Phys. Stat. Solidi (b) **29**, 435 (1968).
[61] P. Blaha, K. Schwarz, G. Madsen, D. Kvasnicka, and J. Luitz, in *Calculating Crystal Properties*, edited by K. Schwarz (Technische Universitat Wien, Wien, 2001).
[62] X. Hong, K. Zou, and J. Zhu, Phys. Rev. B **80**, 241415(R) (2009).
[63] E. H. Hwang and S. Das Sarma, Phys. Rev. B **77**, 195412 (2008).
[64] B. Das, S. Subramaniam, M. R. Melloch, and D. C. Miller, Phys. Rev. B **47**, 9650 (1993).
[65] B. Sadhukhan, S. Bandyopadhyay, A. Nayak, and A. Mookerjee, Int. J. Mod. Phys. B **31**, 1750218 (2017).
[66] K. Fukumoto, K. Onda, Y. Yamada, T. Matsuki, T. Mukuta, S.-I. Tanaka, and S.-Y. Koshihara, Rev. Sci. Instrum. **85**, 083705 (2014).
[67] F. Inuzuka, K. Misawa, K. Nishi, and R. Lang, Appl. Phys. Lett. **85**, 3678 (2004).
[68] K. Bashyal, C. K. Pyles, S. Afroosheh, A. Lamichhane, and A. T. Zayak, J. Phys.: Condens. Matter **30**, 065501 (2018).

[69] F. Oba and Y. Kumagai, Appl. Phys. Express **11**, 060101 (2018).
[70] X. Ma, Y. Wu, Y. Lv, and Y. Zhu, J. Phys. Chem. C **117**, 26029 (2013).
[71] D. Koller, F. Tran, and P. Blaha, Phys. Rev. B **83**, 195134 (2011).
[72] O. Madelung, *Semiconductors: Data Handbook* (Springer, Berlin, 2013).
[73] I. Petousis, D. Mrdjenovich, E. Ballouz, M. Liu, D. Winston, W. Chen, T. Graf, T. D. Schladt, K. A. Persson, and F. B. Prinz, Sci. Data **4**, 160134 (2017).